Temperature dependence of silicon photodiode quantum efficiency: theoretical and experimental results[1]

Thierry Appourchaux, Didier Martin and Udo Telljohann

ESA / ESTEC, P.O. Box 299,
2200AG Noordwijk, The Netherlands

ABSTRACT

The temperature dependence of photodiodes' quantum efficiency for different processes (deep diffused and ion implanted) and resistivities (10 and 100 Ω.cm) were measured. To better predict their behaviour, a comparison was made with a simple uni-dimensional *p-n* junction model. This includes band-gap, depletion region width, diffusion constants, mobilities, intrinsic carrier concentration, absorption coefficient and refractive index temperature functions. The surface recombination length of the minority carriers and the concentration of recombination centers were fitted to the experimental data.

1 INTRODUCTION

An instrument dedicated to the detection of solar oscillations is being built in ESTEC for the Variability of solar IRradiance and Gravity Oscillations (VIRGO) experiment[1]. VIRGO is to be flown on the ESA/NASA SOlar and Heliospheric Observatory (SOHO) spacecraft[2]. A subunit of this instrument called the Luminosity Oscillations Imager is specifically designed to detect low frequency solar intensity fluctuations[3]; periods and amplitudes are of the order of one hour and a few parts per million, and therefore require stable instrumentation. The solar light is analysed with a 5-nm passband filter centered at 500 nm , and detected by a silicon diode array which has 16 pixels.

To simplify the instrumentation, it was chosen not to control the temperature of the detector. This passive control is possible because the distance to the Sun and the solar aspect angle of the SOHO satellite does not vary much during the mission[2]; temperature variations should be at the most 1 K. Since the instrument detects solar intensity fluctuations, it is extremely important to have a silicon photodiode with a quantum efficiency as insensitive as possible to temperature fluctuations. In order to find such a photodiode, we planned to obtain different types of silicon photodiodes and to measure the temperature dependence of their quantum efficiency (TDQ).

We will first describe the silicon detector and the different fabrication processes. We will then expose the experimental set-up, and then its associated results. We will finally interpret the data with a model we developed. We will discuss how to improve the model and what can be the applications of silicon detectors with a low TDQ. We will finally conclude by summarizing the most important points of this study.

2 DETECTOR DESCRIPTION

Four processes were used: Deep diffused and ion implanted, each with two resistivities: 10 Ohm.cm and 100 Ohm.cm. We were supplied, for each process, with 2 detectors without a window. In total, 8 detectors made by the Norwegian company AME were tested. Each detector is made up of 16 pixels (Fig 1). There are 12 pixels dedicated to the scientific signals and 4 pixels for the guiding. This optimum configuration is derived from the need to detect low degree solar oscillations while also providing a signal to accurately position the Sun's image on the detector[4]. In addition, there are four blackened diodes which are used as temperature sensors of the substrate. They also give an indication of the temperature gradients on the detector. They will eventually be used in flight to remove the temperature effects on the detected signals.


Figure 1: Detector optimized for detection of low degree solar oscillations. The four guiding pixels are 90° sectors of an annulus. They are aligned with the solar rotation axis and equator; they all have the same surface. Their inner radius is 5.8 mm and the outer radius is 6.4 mm. The parameter a is half the solar radius (a=3.055 mm). The four black spots at the corners are the temperature diodes. The North-South (N-S) pixels are the 4 ones at the top and bottom. The East-West (E-W) pixels are the 4 ones at the left and right. The Central (C) pixels are the 4 ones in the center
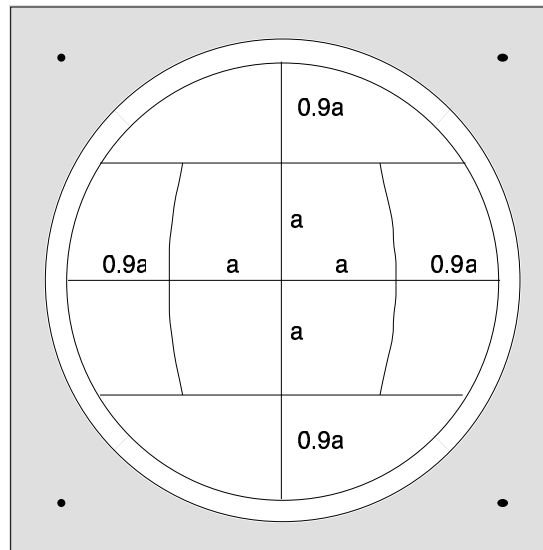
3 MEASUREMENTS

The quantum efficiency of the detectors was derived, at a given temperature, by measuring the response of the photodiodes for different light fluxes, i.e. the current (A) as a function of the light flux (W/cm^2). The response is calibrated in terms of number of electrons generated per number of photons incident on the detector. The TDQ is then obtained by varying the temperature of the detector.

Figure 2: Optical set-up for determination of the quantum efficiency of the photodiodes and its temperature dependence. Lenses are represented by ellipses.
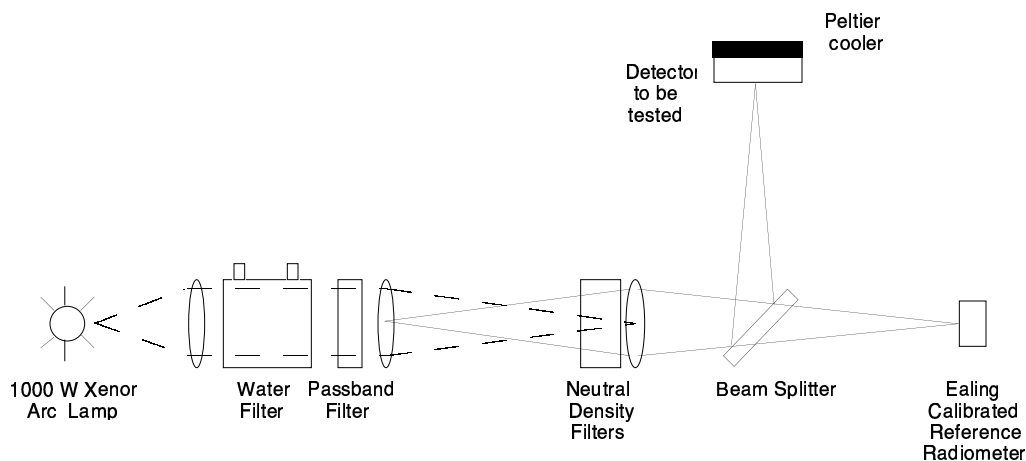
The optical set-up is shown on Fig. 2. It consists of an Oriel Xenon lamp giving a collimated beam with a condenser. The beam shines through an infrared blocking water filter cooled by running water, and then through a 40-nm passband filter; there are 7 filters covering the wavelengths from 0.4 μm to 0.7 μm by steps of 0.05 μm. A field lens located at the filter images the lamp onto a neutral density filter. The neutral density filters are located in 2 filter wheels which allow the selection of 7 densities ranging from 0 to 3 by steps of 0.5. An other field lens located close to the filter wheel (and the lamp image) images the filter onto the detector to be tested; the size of the image is about 30 mm in diameter. The inhomogeneities of the image flux, integrated over a pixel, are about 3% p-p. Lamp fluctuations are of the order of 1% p-p. Inhomogeneities fluctuations are about 0.1% p-p. The filter is also imaged onto an Ealing reference radiometer. This radiometer has a calibration traceable to the NBS, and its spectral response is almost flat from 400 nm to 1000 nm; light flux can be as high as 1 mW/cm^2 at 500 nm with a 40-nm passband filter. The radiometer has an effective surface area of 38 mm^2 and samples the 4 central pixels of the detector. This latter is mounted on a Peltier cooler which can change its temperature from 5 $^{\circ}$C to 45 $^{\circ}$C. The temperature of the substrate is

measured with the four temperature diodes which were previously calibrated for all the detectors. Not shown on Fig. 2 is the purging with dry air of the box containing the detector, which had to be done in order to prevent water condensation on the detector during cooling. The radiometer is at room temperature which is controlled by an air conditioner; fluctuations could be up to 0.5 K p-p during a single test. This effect could account for a maximum 1% systematic error in the measurement of the TDQ. The detectors can be exchanged without modifying the optical path.

Figure 3: Electronics set-up for automated measurements of the quantum efficiency of the photodiodes and their temperature dependence.
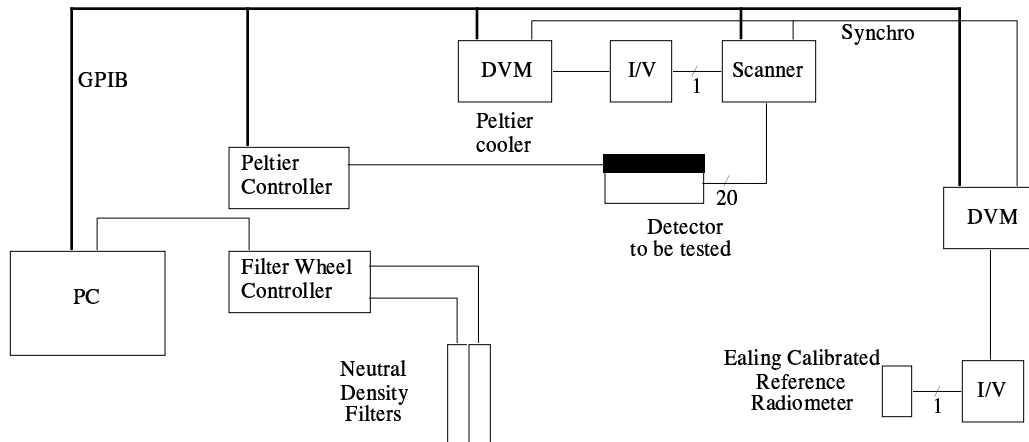
The electronic set-up is given in Fig. 3. All the pixels of the detector under test are connected to a scanner which enables us to measure the pixels one by one, grounding the others in order to reduce current injection from neighbouring pixels. The output of the scanner is connected to an amplifier which converts the photocurrent into a voltage which is then measured by a high precision Digital Voltmeter (DVM). The radiometer is permanently connected to the same type of amplifier whose output is sampled by the same type of precision voltmeter. All the instruments are controlled by a PC either via GPIB or dedicated I/O cards, allowing a fully automated measuring sequence. The programme scans all the pixels sequentially for the different light fluxes and temperatures. Calibration errors due to lamp fluctuations were reduced to 0.1% p-p by averaging 10 measurements and synchronising the pixel and reference readings.

Figure 4: Temperature dependence of the quantum efficiency of the photodiodes at 500 nm as a function of the process and of the type of pixels. Each data point is an average over the 4 pixels which have the same shape. Error bars are ±1σ value.
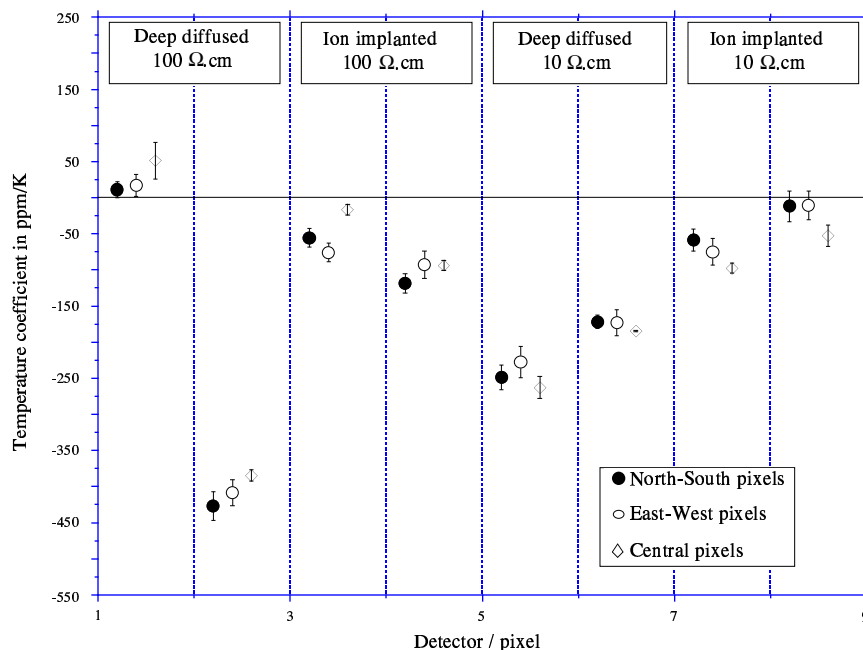
The data reduction was performed as follows: for each pixel of a detector, and at a given temperature, we fit a first order polynomial to the response curve; there is no need to fit a second order polynomial because photodiodes are highly linear devices. We used a weighted least square analysis because the relative error bars on the current of a pixel are proportional to the lamp fluctuations. The slope of the fit, in $A/(W/cm^2)$, is then converted to the quantum efficiency by calibrating the optical path with the reference detector, and by using the measured surface of the pixel (which is 8.63 mm^2, 7.24 mm^2 or 8.29 mm^2 respectively for the N-S, E-W and C pixels). The absolute calibration is accurate within ±5% and is mainly due to the error made in calibrating the optical path; reproducibility of this calibration is also within ±5%. For all the pixels but the guiding ones the quantum efficiency for the different pixels shape agree within 1%; this means that the effective area of a pixel is very close to its physical area. The discrepancy for the guiding pixels comes from a lack of metallization outside the sensitive area. A first order fit of the quantum efficiency as a function of temperature was then performed. The fit is unweighted since the error bars on all measurements are similar. The slope divided by the quantum efficiency at 0 ^{o}C gives TDQ. Figure 4 shows the results at 500 nm for all the processes and all the pixels but the guiding ones. We deduced that TDQ is insensitive to the pixel shape or size. The spread of TDQ is also much larger for the deep diffused process than for the ion implanted one. For the ion implanted, TDQ seems to be insensitive to the substrate resistivity; we can expect a TDQ not larger than 100 ppm/K with this process. To better understand the behaviour of the TDQ, we also measured its dependence as a function of wavelength. The measurement of the quantum efficiency was performed at the same time. As we showed in figure 4 that the TDQ is not a function of pixel shape or size, and since the measurements are quite time consuming, only one detector per process was measured and only its four Central pixels were used. Figure 5 shows the measured quantum efficiency for the 4 processes. The quantum efficiency is rather insensitive to the substrate resistivity. The ion implanted process shows a much better response in the blue than the deep diffused. Again differences are much larger for the deep diffused process than for the ion implanted; this is because the former fabrication process is much more difficult to control; ion implantation allows to dope the p region much more precisely.
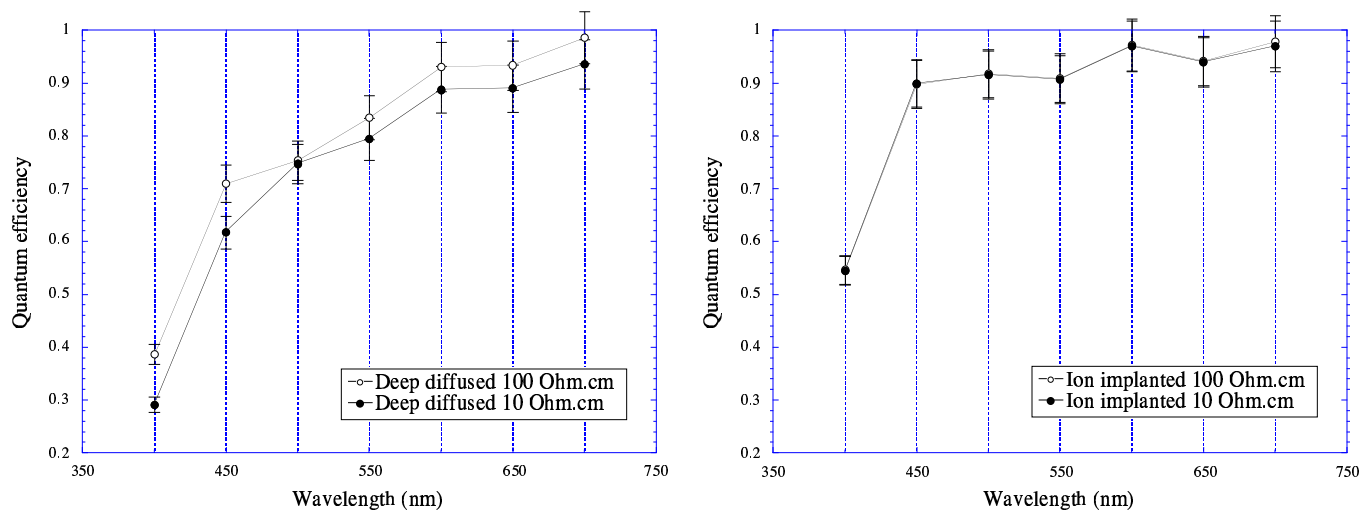

Figure 5: Quantum efficiency as a function of wavelength for the deep diffused (left) and ion implanted (right) detectors. Error bars are ±5%.

Figure 6 show the measured TDQ for the 4 processes. For the deep diffused, it can easily be deduced that the TDQ becomes much worse in the blue (about 1000-2000 ppm/K), whereas it tends to be much less in the red. For the ion implanted the TDQ has a minimum around 450-500 nm of about -100 ppm/K.
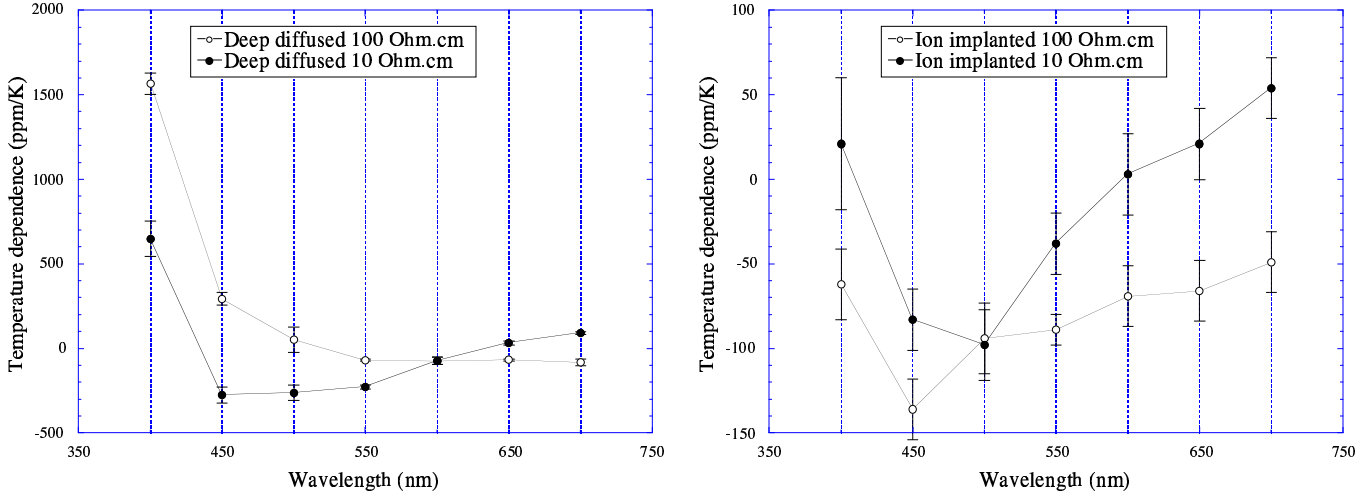
Figure 6: Temperature dependence of the quantum efficiency as a function of wavelength for the deep diffused (left) and ion implanted (right) detectors. Error bars are ±3σ.

4 MODELLING

We are considering the photodiode structure of Fig. 7. All depths are referenced to the diode's surface. The metallurgical junction is located at x_j. The front region doping is given by the acceptor atom concentration N_a, the back region doping by the donor atom concentration N_d. As light penetrates the silicon photodiode, photons get absorbed and excite electrons from the valence band into the conduction band, effectively creating an electron hole pair. Due to the diode effect, electrons and holes are separated. The minority carriers diffuse towards the junction but during this process they can be absorbed by either surface recombination or bulk recombination because of their finite lifetimes. Hence each created electron hole pair is not necessarily collected at the diode terminals. The internal quantum efficiency of a diode is defined as the ratio between the number of collected electrons to the number of photons incident on the actual diode[9].

Figure 7: Photodiode structure. Front region is p type, back region n type. The hatched area represents the layer of silicon dioxide (of thickness d_2) which acts as a passivation layer and as an anti-reflection coating.
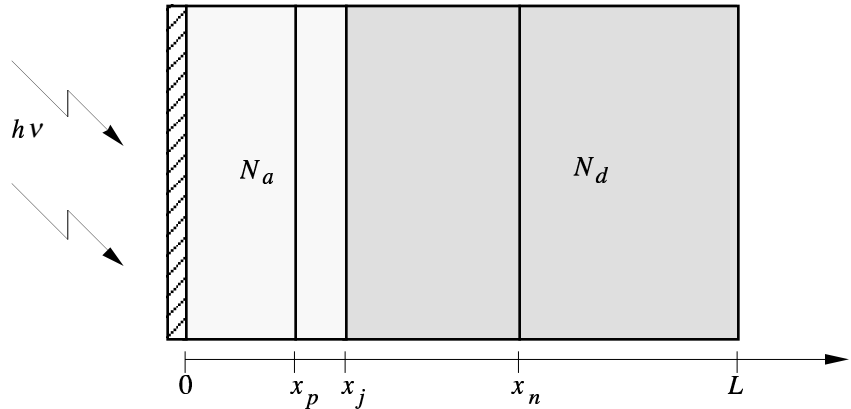
In establishing the theoretical internal quantum efficiency (η), the following approximations have been made:

- each absorbed photon creates an electron-hole pair, i.e. the quantum yield is unity, and the optical generation of carriers occurs by band to band transitions, so that electron and hole generation rates are equal.
- a uni-dimensional p-n junction model is used.
- the diode is assumed to have an abrupt doping profile and the depletion region approximation was made. Hence the diode could be split into three regions, two quasi neutral regions ($0 < x < x_p$ and $x_n < x < L$) in

which the electric field was neglected and a depletion region ($x_p<x<x_n$) in which no recombination of carriers is supposed to occur due to the presence of a high electric field.
- the Shockley-Read single recombination level model is used[9]
- the low injection case is assumed so as to not deviate too much from the equilibrium state. This means low illumination level.
- non-degenerate semiconductors are used

The quantum efficiency (Q) can be calculated as the product of the internal quantum efficiency (η) by the transmission coefficient (T) of the air-SiO$_2$-Si interface, respectively given in sections 8.1 and 8.2. All the parameters, such as the absorption coefficient α, the diffusion lengths, the depletion region width, the bandgap energy and the refractive index of silicon appearing in the analytical expression of Q are given with their temperature dependence in the appendix 8.

5 INTERPRETATION OF DATA AND DISCUSSION

In the model described in section 4, the impurity concentrations N_a (=10^{18} cm^{-3}), N_d (=5 10^{13} cm^{-3} for the 100 Ohm.cm substrates and 5 10^{14} cm^{-3} for the 10 Ohm.cm substrates), the junction depth x_j (=4.5 μm for the deep diffused, 0.15 μm for the ion implanted 100 Ohm.cm and 0.13 μm for the ion implanted 10 Ohm.cm prototypes) as well as the oxide layer thickness d_2 (=90 nm) were specified by AME, the other parameters were unknown. The concentration of recombination centers N_r (giving the diffusion length L_n) and the surface recombination velocity s, or equivalently, recombination length L_s, were used to fit the theoretical curves to the measured data. Figure 8 compares the measured quantum efficiency to our theory.
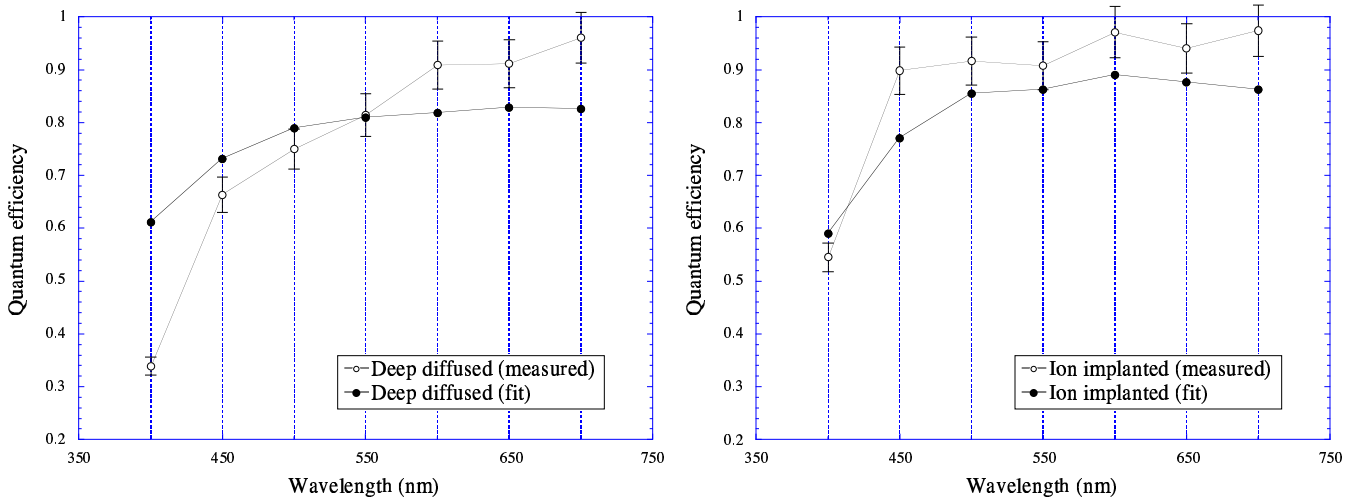

Figure 8: Measured and fitted quantum efficiency as a function of wavelength for the deep diffused (left) and ion implanted (right) detectors. Error bars are ±5%.

The optimum value for N_r was 4.0 10^{13} ± 2.5 10^{12} cm^{-3} for the deep diffused process and 1.4 10^{17}± 7.8 10^{15} cm^{-3} for the ion implanted. As can be seen on these curves, it was rather difficult to simulate the rapid decrease of Q in the blue. This might be due to a problem in the modelling of the absorption coefficient, more specifically in the threshold energies of the various absorption processes. Indeed, a second indirect absorption mechanism comes into play for wavelengths shorter than 500nm (Rajkanan[6] specifies a threshold energy for this mechanism of ±2.5eV) and around 400nm the absorption coefficient rises rapidly because of a direct absorption (threshold energy: ±3.2eV). Although figure 8 shows a systematic under-estimation of Q by 5%, which is probably due to an absolute calibration error in our measurements, the fit for the ion implant process seems to work better than for the diffusion process. The most probable reason for this is that the front region for the ion implant process is much narrower (0.15 μm) than for the deep diffused one (4.5 μm). Hence, in the former case the depletion region plays a major role in the absorption of light. For the latter, the front region is more important and the model for this region seems to be inaccurate. Indeed, because of the doping gradient within this zone (as compared to our assumption of an abrupt doping profile), an

electric field will be present and enhance the quantum efficiency. Our model tries to compensate for this error by using a larger diffusion length in the p region. We have also used a model which incorporates an average electric field in the front region[9] and although this seemed to work a bit better, it was still not very satisfying. The only solution to this problem would be to use a finite element programme and include a more realistic doping profile. From our results, we could see that the surface recombination velocity had only a small influence on the quantum efficiency and it was the concentration of recombination centers N_r which played a major role in the fits.

The same type of fits were performed for the TDQ. The results are summarized in figures 9 and 10. For all the fits L_s was taken to be very large. Variations with temperature of the silicon complex index of refraction $n_3 + ik_3$ were taken from tabulated data[10] and included in the evaluation of the transmission coefficient T. For the deep diffused process, the best agreements were obtained with an N_r of $8.0\ 10^{13} \pm 1.5\ 10^{12}$ cm^{-3} and $1.1\ 10^{16} \pm 3.2\ 10^{14}$ cm^{-3} for the 100 Ohm.cm and 10 Ohm.cm substrates respectively. For the 10 Ohm.cm substrates, a reasonable fit was only possible by reducing the junction depth to 0.57 ± 0.006 μm, again showing the problem we faced with the inaccurate modelling of the front region. For the TDQ we also tried the model including an average electric field in the front region but without success this time.
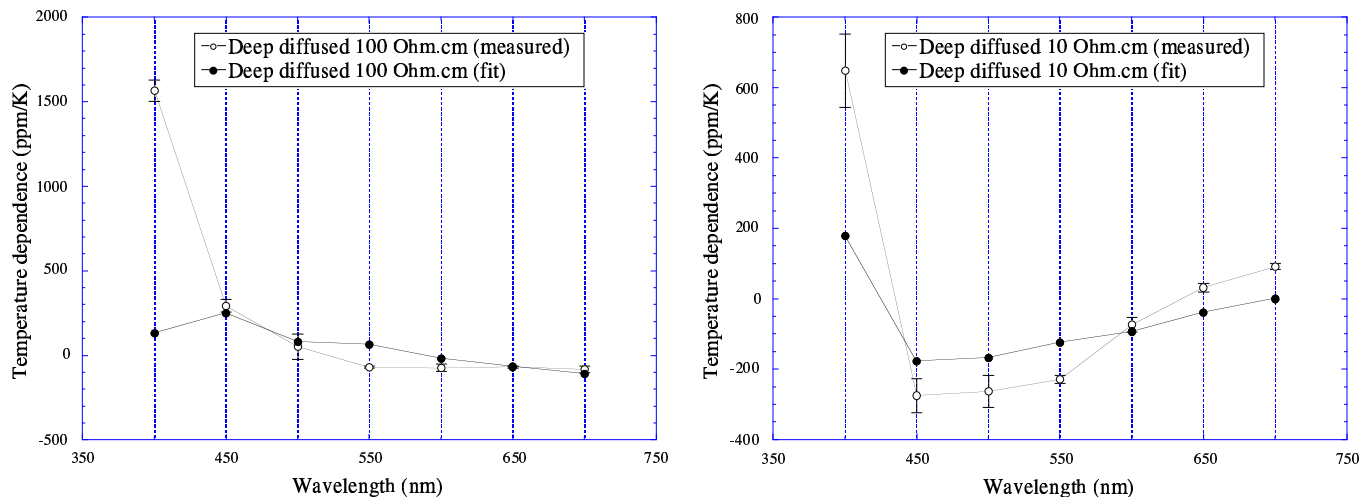

Figure 9: Measured and fitted TDQ as a function of wavelength for the deep diffused 100 Ohm.cm (left) and deep diffused 10 Ohm.cm (right) detectors. Error bars are ±5%.
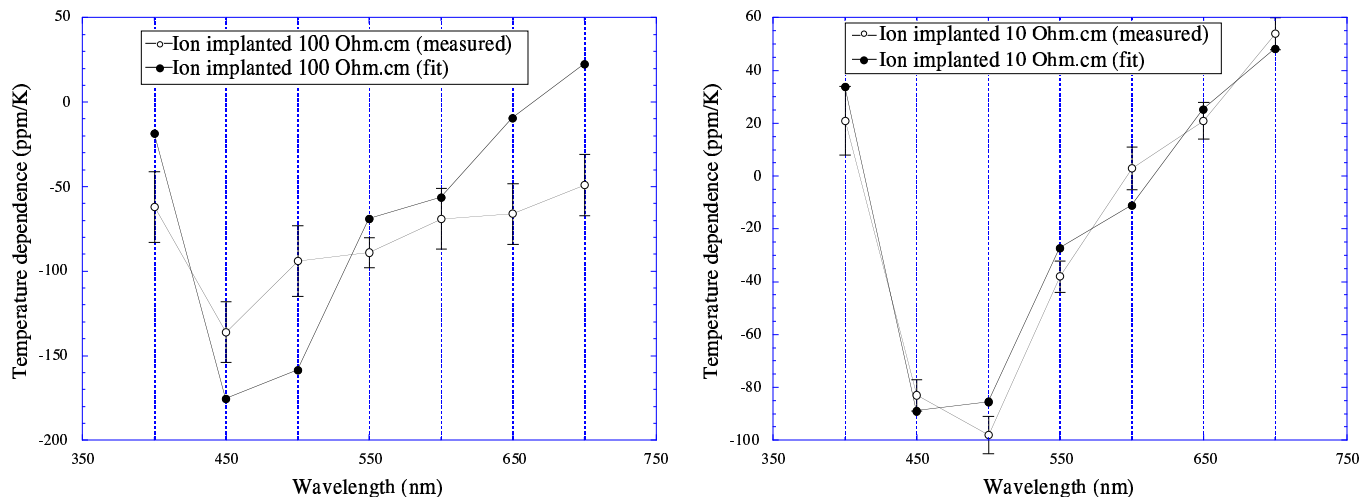

Figure 10: Measured and fitted TDQ as a function of wavelength for the ion implanted 100 Ohm.cm (left) and ion implanted 10 Ohm.cm (right) detectors. Error bars are ±5%.

Our best achievement is with the ion implant process (figure 10). An N_r of 1.77 $10^{16} \pm 4.8$ 10^{14} cm^{-3} and 1.9 $10^{16} \pm 1.7$ 10^{15} cm^{-3} were obtained for the 100 Ohm.cm and 10 Ohm.cm substrates respectively. These two values are perhaps relatively high but consistent with each other. The process of ion implantation probably creates more dislocations and energy traps than a diffusion process. For these rather good fits, we had to change the junction depths (as given by the manufacturer to be 0.15 and 0.13 µm) into 0.44 and 0.36 µm respectively. Finally the influence on TDQ of the temperature variation of the oxide layer thickness d_2, the extension of the depletion region in the p zone x_p and the surface recombination length L_s were shown to be negligible.

6 CONCLUSION

We measured the quantum efficiency and the temperature dependence (TDQ) of silicon photodiodes as a function of wavelength; the detectors were made out of 4 different processes. Quantum efficiency ranged from 0.4 to 0.9 with a ±5% precision. The TDQ ranged from -150 ppm/K to 1500 ppm/K with a precision ranging from 5 to 20 ppm/K (1σ value). We modelled the behaviour of the quantum efficiency and its TDQ by fitting two parameters: the surface recombination length and the number of recombination centers. We showed that the surface recombination length was not a critical parameter and that temperature dependences of the silicon dioxide layer thickness d_2 and the extension of the depletion region in the p zone x_p had very little influence on Q and, hence, could be neglected in TDQ. The major contributions to TDQ came from the temperature dependences of the absorption coefficient α, the diffusion length of minority carriers $L_{n,p}$ (especially in the front region) and the complex refractive index of silicon $n_3 + ik_3$. In some cases an average electric field in the front region was also fitted. We found that the results for the ion implanted process could be easily explained by a uni-dimensional model of an abrupt junction. The same model did not work on the deep diffused process. It was not possible to reproduce the drop at 400 nm of the quantum efficiency. Furthermore, to obtain the measured TDQ at this wavelength we had to introduce a higher temperature dependence of the diffusion length of the holes which bears no relationship to the physics of the semiconductor. The discrepancies could be reduced by using a finite element model of the photodiode, and by introducing a more realistic doping profile. The simple model could be used, within given limits, to predict the TDQ and quantum efficiency of CCDs used to perform high precision photometry on stars[15]. Especially surface CCD's could be modelled quite well because of the absence of a differently doped front region.

7 ACKNOWLEDGMENTS

8 APPENDIX

8.1 Internal quantum Efficiency

The total internal quantum efficiency (η) of a photodiode can be expressed as the sum of the partial quantum efficiencies in each of the considered regions and are given by[9]:

$$\eta_p = \frac{\alpha L_n^2}{1 - \alpha^2 L_n^2} \left\{ \alpha\, e^{-\alpha x_p} - \frac{1}{L_n} \frac{L_n(1+\alpha L_s) - e^{-\alpha x_p}\left(L_n \cosh\left[x_p/L_n\right] + L_s \sinh\left[x_p/L_n\right]\right)}{L_n \sinh\left[x_p/L_n\right] + L_s \cosh\left[x_p/L_n\right]} \right\}$$

8.1.1

$$\eta_{dr} = e^{-\alpha x_p} - e^{-\alpha x_n}$$

8.1.2

$$\eta_n = \frac{\alpha L_p^2}{1 - \alpha^2 L_p^2} \left\{ \alpha\, e^{-\alpha x_n} - \frac{e^{-\alpha L} - e^{-\alpha x_n} \cosh\left[(L-x_n)/L_p\right]}{L_p \sinh\left[(L-x_n)/L_p\right]} \right\}$$

8.1.3

In which η_p, η_{dr} and η_n are respectively the contribution of the p, depletion and n regions, α is the absorption coefficient of silicon (see section 8.5), L the thickness of the photodiode, L_n and L_p the diffusion lengths of electrons and holes respectively (see section 8.3 and 8.4) , x_n and x_p the depletion layer limits on the n and p side respectively and L_s the surface recombination length. The diffusion length are related to the carrier lifetime $\tau_{n,p}$ and diffusion constant $D_{n,p}$ as:

$$L_{n,p} = \sqrt{\tau_{n,p}D_{n,p}}$$

8.1.4

Expressions of the minority carrier lifetime and diffusion constant can be found in section 8.3 and 8.4. The parameter L_s is the surface recombination length and is a function of the surface recombination velocity s :

$$L_s = \sqrt{\frac{D_n}{s}}$$

8.1.5

The parameters x_n and x_p (in cm) are given by:

$$x_p = x_j - \sqrt{\frac{2\varepsilon_{Si}\varepsilon_o}{q}\frac{N_d}{N_a(N_a+N_d)}}\sqrt{\phi_o - V}$$

8.1.6

$$x_n = x_j + \sqrt{\frac{2\varepsilon_{Si}\varepsilon_o}{q}\frac{N_a}{N_d(N_a+N_d)}}\sqrt{\phi_o - V}$$

8.1.7

$$\phi_o = \frac{k.T}{q}.ln\left(\frac{N_a.N_d}{n_i^2}\right)$$

8.1.8

where x_j is the junction depth (in cm), ε_o is the free space permittivity (=8.85 10^{-14} F/cm), ε_{Si} the relative permittivity of silicon[14] (=11.7), q is the charge of the electron, N_a and N_d are the acceptor and donor concentration in cm^{-3}, ϕ_o is the internal barrier potential and V the external applied voltage (=0 for photodiodes in photocurrent mode). The intrinsic carrier concentration (in cm^{-3}) is taken to be[7]:

$$n_i = 5.931\ 10^{15}T^{3/2}exp\left(\frac{- E_g(T,C_c)}{2kT}\right)$$

8.1.9

where the band gap is also a function of carrier concentration C_c (in cm^{-3}) and temperature[7]:

$$E_g(T,C_c) = E_{g,o} - \frac{7.021\ 10^{-4}T^2}{T+1108} - 0.389\left(\frac{C_c}{10^{18}T}\right)^{1/2}$$

8.1.10

$$E_{g,o} = 1.1557\ eV$$

8.2 Transmission coefficient

The reflection and transmission coefficients for a three layer structure can be easily calculated and has been studied previously[8]. For our purposes, the first medium is air, the second one, of thickness d_2, is silicon dioxide and the third layer is pure silicon. If the indices refer to the respective layers, the transmission coefficient into the silicon is given by:

$$T = \frac{n_3}{n_1}\frac{(1+r_2)^2\left[(1+g_3)^2+h_3^2\right]}{1 + r_2^2(g_3^2+h_3^2) + 2r_2\left[g_3cos(2\delta_2)+h_3sin(2\delta_2)\right]}$$

8.2.1

where,

$$\delta_2 = \frac{2\pi n_2 d_2}{\lambda}$$

$$\text{8.2.2}$$

$$r_2 = \frac{n_1 - n_2}{n_1 + n_2}$$

$$\text{8.2.3}$$

$$g_3 = \frac{n_2^2 - n_3^2 - k_3^2}{(n_2 + n_3)^2 + k_3^2}$$

$$\text{8.2.4}$$

$$h_3 = \frac{2 n_2 k_3}{(n_2 + n_3)^2 + k_3^2}$$

$$\text{8.2.5}$$

where n_1 is the refractive index of air (=1), n_2 the refractive index of silicon dioxide (=1.46), $n_3 + i k_3$ the complex refractive index of silicon[10], d_2 silicon oxide thickness (in our case about 90 nm for optimization at 500 nm).

8.3 Minority carrier lifetime

Minority carrier lifetime has been treated in earlier papers[7], the results are summarized here. The excess carrier lifetime τ is related to the excess carrier concentration n' (in cm^{-3}) and its recombination rate R (cm^3 s^{-1}) as follows:

$$\tau = \frac{n'}{R}$$

$$\text{8.3.1}$$

$$n' = \frac{1}{2}\left[\left\{ (N_a - N_d)^2 + 4 n_i^2 \exp\left(\frac{E_{Fn} - E_{Fp}}{kT}\right) \right\}^{1/2} - \left\{ (N_a - N_d)^2 + 4 n_i^2 \right\}^{1/2} \right]$$

$$\text{8.3.2}$$

$$R = \frac{N_r \sigma v}{2\delta} \frac{kT n_i^2 \left[\exp\left(\frac{E_{Fn} - E_{Fp}}{kT}\right) - 1 \right]}{\left[(N_a - N_d)^2 + 4 n_i^2 \left\{ \exp\left(\frac{E_{Fn} - E_{Fp}}{kT}\right) - 1 \right\} \right]^{1/2}} \ln \left[\frac{X + Y \tanh\left|\frac{E_a + \delta}{2kT}\right|}{X - Y \tanh\left|\frac{E_a + \delta}{2kT}\right|} \frac{X - Y \tanh\left|\frac{E_a - \delta}{2kT}\right|}{X + Y \tanh\left|\frac{E_a - \delta}{2kT}\right|} \right]$$

$$\text{8.3.3}$$

Where,

$$X = \left\{ (N_a - N_d)^2 + 4 n_i^2 \exp\left(\frac{E_{Fn} - E_{Fp}}{kT}\right) \right\}^{1/2} + 2 n_i$$

$$\text{8.3.4}$$

$$Y = \left\{ (N_a - N_d)^2 + 4 n_i^2 \left[\exp\left(\frac{E_{Fn} - E_{Fp}}{kT}\right) - 1 \right] \right\}^{1/2}$$

$$\text{8.3.5}$$

where σ is the electron and hole capture cross section (=10^{-15} cm^2), v the thermal velocity of carriers (in cm/s), N_r the density of recombination centers in cm^{-3}, E_a energy distribution parameter (=0.2 eV), δ energy distribution parameter (=0.2 eV), $E_{Fn,Fp}$ quasi Fermi level for electrons and holes. Since we are considering the low injection case, we take the quasi Fermi levels to coincide with the equilibrium Fermi level, hence their difference is taken to be zero. The intrinsic carrier concentration is given by formula 8.1.9.

8.4 Diffusion constant

Diffusion constant has also been modelled by Singh and Singal[7]. It is related to the mobility by Einstein's relation:

$$D_{n,p} = \frac{kT}{q} \mu_{n,p}$$

<div align="right">8.4.1</div>

The mobility of carriers is limited by three processes: lattice, impurity and carrier scattering. For the impurity and carrier scattering contributions, some discrepancies were found between the various references[7,11,13,14]. The formulas we used in our model, where μ are given in $m^2.V^{-1}.s^{-1}$ are the following:

$$\mu = \left[\frac{1}{\mu_l} + \frac{1}{\mu_i} + \frac{1}{\mu_c}\right]^{-1}$$

<div align="right">8.4.2</div>

$$\mu_{l,n} = 2.1 \; 10^9 \; T^{-2.5}$$

<div align="right">8.4.3</div>

$$\mu_{l,p} = 2.3 \; 10^9 \; T^{-2.9}$$

<div align="right">8.4.4</div>

$$\mu_i = \frac{2^{7/2}(\varepsilon_{Si}\varepsilon_o)^2(kT)^{3/2}}{\pi^{3/2}C_i q^3 m_{eff}^{1/2} ln\left\{\left(3\varepsilon_{Si}\varepsilon_o C_i^{1/3}\frac{kT}{q^2}\right)^2 + 1\right\}}$$

<div align="right">8.4.5</div>

$$\mu_c = \left(\frac{1}{m_n} + \frac{1}{m_p}\right)^{1/2} \frac{3(\varepsilon_{Si}\varepsilon_o)^2(kT)^{3/2}}{2^{3/2}\pi^{1/2}C_c q^3 ln\left\{\left(4\varepsilon_{Si}\varepsilon_o C_c^{1/3}\frac{kT}{q^2}\right)^2 + 1\right\}}$$

<div align="right">8.4.6</div>

where ε_o is the free space permittivity in F/m, C_i and C_c are respectively the impurity and carrier concentration in m^{-3} (in both case they are $10^6 N_a$ in p region, $10^6 N_d$ in n region), m_{eff} the effective carrier mass ($9.8 \; 10^{-31}$ kg), m_n the effective electron mass[11] ($=0.26 m_{eff}$), m_p the effective hole mass[11] ($=0.37 m_{eff}$)

8.5 Absorption coefficient

The absorption process in silicon is quite complex since both direct and indirect transitions (involving absorption and emission of phonons) occur. An expression of the absorption coefficient (in cm^{-1}) as a function of incident wavelength, band gap energy and temperature is given by[6]:

$$\alpha(T) = \sum_{\substack{i=1,2 \\ j=1,2}} C_i A_j \left[\frac{\{E - E_{gj} + E_{pi}\}^2}{\left\{exp\left(\frac{E_{pi}}{kT}\right) - 1\right\}} H(E - E_{gj} + E_{pi}) + \frac{\{E - E_{gj} - E_{pi}\}^2}{\left\{1 - exp\left(\frac{-E_{pi}}{kT}\right)\right\}} H(E - E_{gj} - E_{pi})\right]$$

$$+ A_d \left[E - E_{gd}\right]^{1/2} H(E - E_{gd})$$

<div align="right">8.5.1</div>

where E_{g1}, E_{g2} and E_{gd} are given by 8.3.7, where $E_{g,o}$ is replaced by 1.1557, 2.5 and 3.2 eV respectively, and E is the photon energy in eV, E_{p1} the phonon energy mode TA ($=0.01827$ eV), E_{p2} the phonon energy mode TO ($=0.05773$ eV), $C_1=5.5$, $C_2=4.0$, $A_1=323.1$ $cm^{-1}eV^{-2}$, $A_2=7237$ $cm^{-1}eV^{-2}$, $A_d=1.052 \; 10^6$ $cm^{-1}eV^{-2}$, and $H(x)$ is the Heaviside function ($H(x) =1$ for $x \geq 0$, $H(x) =0$ $x<0$).

9 REFERENCES

1 C.FRÖHLICH, B.N.ANDERSEN, G.BERTHOMIEU, D.CROMMELYNCK, P.DELACHE, V.DOMINGO, A.JIMENEZ, A.R.JONES, T.ROCA CORTES and C.WEHRLI, "VIRGO- The Solar Monitor Experiment on SOHO", *The SOHO Mission*, ESA SP-1104, p. 19-23, 1989

2 V.DOMINGO, *The SOHO Mission*, ESA SP-1104, 1989

3 B.N.ANDERSEN, V.DOMINGO, A.R. JONES, A.JIMENEZ, P.L.PALLE, C.REGULO and T.ROCA CORTES, "Luminosity Oscillations Imager (LOI)", *Seismology of the Sun and Sun-like Stars*, ESA SP-286, p. 385-386, 1988

4 T.APPOURCHAUX and B.N.ANDERSEN, "Observations of Low-Degree Solar Oscillations with Few Detector Elements", *Solar Physics*, **128**, p. 91-110, 1990

5 G.ROLLAND, "Etude des Variations de Rendement Quantique Interne d'un Détecteur CCD en Fonction de la Température", *Revue Phys. Appl.*, **20**, p. 651-659, 1985

6 K.RAJKANAN, R.SINGH and J.SHEWCHUN, "Absorption Coefficient of Silicon for Solar Cell Calculations", *Solid State Electronics*, **22**, p. 793-795, 1979

7 R.V.SINGH and C.M.SINGAL, "Temperature Dependence of the Open-Circuit Voltage of an N^+-P-P^+ Silicon Solar Cell under High Illumination Levels", *Solar Cells*, **10**, p. 155-175, 1983

8 F.VAN DE WIELE, "Anti-Reflection Films and Multilayer Structures", in Proceeding of NATO Advanced Study Institute on Solid State Imaging, Eds P.G.Jespers, F.Van de Wiele and M.H.White, Noordhoff, Leyden, p. 29-45, 1976

9 F.VAN DE WIELE, "Photodiode Quantum Efficiency", in Proceeding of NATO Advanced Study Institute on Solid State Imaging, Eds P.G.Jespers, F.Van de Wiele and M.H.White, Noordhoff, Leyden, p. 47-90, 1976

10 G.E.JELLISON, Jr. and F.A.MODINE, "Optical Functions of Silicon at Elevated Temperatures Determined by Polarization Modulation Ellipsometry", Report ORNL/TM-9718, Oak Ridge National Laboratory, Oak Ridge, Tennessee, 1985

11 A.VAPAILLE, *Physique des Dispositifs à Semiconducteurs: Electronique du Silicium Homogène*, Masson et Cie, Paris, 1970

12 C.L.HEMENWAY, R.W.HENRY and M.CAULTON, *Physical Electronics*, 2nd edition, J.Wiley and Sons, Inc., Toppan Company Limited, Singapore, 1967

13 E.M.CONWELL, "Properties of Silicon and Germanium", *Proc. IRE*, **40**, p. 1327-1357, 1952

14 H.F.WOLF, *Silicon Semiconductor Data*, Eds H.K.Henisch, Pergamon Press, 1969

15 T.APPOURCHAUX, C.CATALA, S.CATALANO, S.FRANDSEN, A.JONES, P.LEMAIRE, O.PACE S.VOLONTE, W.WEISS, "Report on the Assessment Study for PRISMA: Probing Rotation and Interior of Stars: Microvariability and Activity", ESA SCI(91) 5, 1991